A Scanning AC Calorimetry Technique for the Analysis of Nano-Scale Quantities of Materials

A scanning AC calorimetry technique for the analysis of nano-scale quantities of materials

Kechao Xiao[1], John M. Gregoire[2, b)], Patrick J. McCluskey[3, b)], Joost J. Vlassak[1, a)]

[1]*School of Engineering and applied Sciences, Harvard University, 29 Oxford Street, Cambridge, MA 02138, USA*

[2]*Joint Center for Artificial Photosynthesis, California Institute of Technology, 1200 E. California Blvd., Pasadena, CA 91125, USA*

[3]*GE Global Research, One Research Circle, Niskayuna, NY 12309, USA*

Abstract

We present a scanning AC nanocalorimetry method that enables calorimetry measurements at heating and cooling rates that vary from isothermal to 2×10^3 K/s, thus bridging the gap between traditional scanning calorimetry of bulk materials and nanocalorimetry. The method relies on a micromachined nanocalorimetry sensor with a serpentine heating element that is sensitive enough to make measurements on thin-film samples and composition libraries. The ability to perform calorimetry over such a broad range of scanning rates makes it an ideal tool to characterize the kinetics of phase transformations or to explore the behavior of materials far from equilibrium. We demonstrate the technique by performing measurements on thin-film samples of Sn, In, and Bi with thicknesses ranging from 100 to 300 nm. The experimental heat capacities and melting temperatures agree well with literature values. The measured heat capacities are insensitive to the applied AC frequency, scan rate, and heat loss to the environment over a broad range of experimental parameters.

[a)] e-mail address: vlassak@esag.harvard.edu

[b)] This research was performed while the author was at the School of Engineering and applied Sciences, Harvard University, 29 Oxford Street, Cambridge, MA 02138, USA

I. Introduction

Scanning calorimetry is an important tool in materials research. Valuable insight is gained in the behavior of a material by measuring the heat absorbed or released when heating or cooling that material. This technique has long been used to determine phase transformation temperatures, enthalpies, and heat capacities. Measurements at very slow heating and cooling rates allow a material to remain at or near equilibrium and provide information on its thermodynamic properties, while measurements at faster scan rates provide characterization of reaction kinetics [1]. The ability to perform calorimetry measurements at very fast scan rates is interesting also, as it enables the study of metastable phases and more generally of materials far from equilibrium [2-6]. Thus, a scanning calorimetry technique that can operate over a broad range of heating and cooling rates is an attractive and powerful tool for materials researchers.

Traditional scanning calorimetry is well developed. Measurements are performed on bulk materials and provide very precise information on their thermal properties. The scan rate in traditional calorimetry is limited to a maximum on the order of 10 K/min, because of the relatively large sample mass required for these measurements. Nanocalorimetry, by contrast, is not bound by this limitation and can achieve much higher heating and cooling rates. Nanocalorimetry is a novel technique that has developed rapidly in recent years [2, 7]. It enables ultrasensitive calorimetry measurements on very small samples of materials through use of micromachined sensors with vanishingly small thermal mass. The sensitivity of nanocalorimetry sensors makes it possible to perform measurements on thin-film samples and composition libraries [8]. Due to the small thermal mass of sensor and sample, very fast heating can be achieved. For instance, the nanocalorimetry sensor originally developed by Allen and coworkers [9] can attain heating rates as large as 10^5 K/s, extending the maximum heating rate of traditional calorimetry by many orders of magnitude. However, the small thermal mass also presents a problem – the measurements are very sensitive to heat loss and the requirement of adiabatic measurement conditions limits the scan rate to this very fast regime. The fraction of input power that is lost to heat must be small, placing a lower bound on the heating rate, which is 10^4 K/s for the calorimetry sensor developed by Allen and colleagues [9]. Schick et al have developed a sensor that can operate under non-adiabatic conditions with controlled heating and cooling rates in the range of 10^3 K/s [10], but its accuracy degrades at lower heating rates.

The issue of heat loss in nanocalorimetry at slow scanning rates can be addressed through use of alternating current (AC) techniques. AC calorimetry is well known as a sensitive technique for measuring thermo-physical properties of materials in the presence of heat loss [11-13], and is thus often applied in isothermal measurements. In AC calorimetry, an oscillating heat input is supplied to the sample and the resulting temperature oscillation is measured [13]. The amplitude and phase lag of the temperature response provide accurate information on both the heat capacity of the sample and its heat loss to the environment. Specifically, the out-of-phase component of the temperature oscillation provides information on the heat capacity of the sample, while the in-phase component is associated with heat losses and irreversible processes. If the oscillation frequency is high enough, the contribution of the heat loss vanishes and the measurement can be regarded as adiabatic.[13] When AC calorimetry is applied to bulk materials, the relevant frequency range is quite low (~1 Hz), because of the finite size of the sample and the thermal resistance between the sample, heater, and thermometer [14]. Indeed, the low frequency increases the thermal diffusion length and ensures that the entire sample is subjected to the maximum temperature oscillation, essential to obtaining accurate heat capacity measurement. The low frequency also sets an upper limit on the scanning rate to ensure that the mean temperature of the sample does not change significantly during a single temperature oscillation [14].

When applied to nanocalorimetry, the reduced thermal time scales expand the applicable frequency range. Schick and colleagues have developed an AC calorimeter for measurements on nano-scale materials using a commercial sensor from Xensor Integration [15]. In this device, the applied AC frequency is limited to approximately 100Hz because the distance between the sample and the temperature sensor dampens the temperature response of the sensor [16]. Moreover, the scan rate cannot exceed 5 K/min because of considerations of temperature uniformity across the sample and accuracy of the temperature measurements [15].

In this paper, we present a scanning AC nanocalorimetry method that enables AC measurements at heating and cooling rates that vary from isothermal to 2×10^3 K/s (and possibly higher) – in terms of scan rate, the technique bridges the gap between nanocalorimetry and traditional scanning calorimetry of bulk materials. To the best of our knowledge, it is the first method to raise the maximum scan rate for AC calorimetry to the 10^3 K/s level. The method is developed and tested using the parallel nano scanning calorimeter (PnSC) device developed by McCluskey

et al. [8, 17], a device designed specifically for calorimetry measurement on nanoscale materials in a high-throughput methodology. Compared to the Xensor device, the PnSC has a much smaller thermal impedance between heater, thermometer, and sample, resulting in a much faster temperature response and much higher accessible AC frequencies. These attributes enable adiabatic operation of the device in a high heat loss environment over a broad range of scan rates.

The main text of this paper is organized into four sections. In Section 2, we present an in-depth analysis of scanning AC calorimetry measurement. In Section 3, we introduce the PnSC device used for the measurement and address issues related to temperature uniformity across the sample region. In Section 4, we describe the experimental set-up and discuss selection of the experimental parameters. In Section 5, we present experimental results for measurements on Sn thin-film samples for a range of frequencies and scan rates.

II. Scanning AC calorimetry

The application of AC calorimetry to measurements, in which the temperature is slowly ramped up, has been used in the past to investigate bulk materials [13, 18-20]. Here we apply the technique to nanocalorimetry. Because of the specific geometry of the nanocalorimetric sensor and the fast scanning rates, the conditions under which valid measurements can be performed need to be determined. Hence we briefly review the theory of AC calorimetry and adapt it to the specifics of the nanocalorimetry sensor used in the PnSC device.

Consider a nanocalorimetry sensor that consists of a heating element with a temperature-dependent resistance. A sample of interest is placed on the sensor and is heated by sending a current through the heating element. The temperature of the sensor is determined by monitoring the resistance of the heater using a four-point measurement scheme (Fig. 1). In the analysis, we assume that the temperature is uniform across the heating element and that the temperature difference between the heating element and the sample is negligible. The first assumption will be analyzed in more detail in the next section. The second assumption is valid as long as the thermal diffusion length is much larger than the sensor thickness at the time scale of the measurements and this is indeed the case for the sensors under consideration [8].

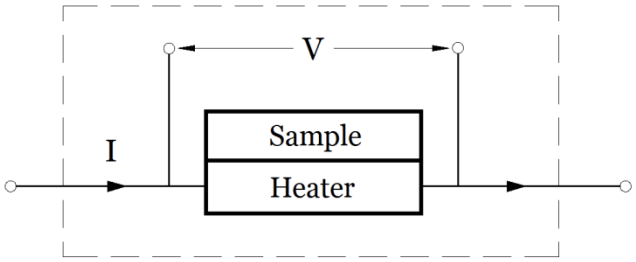

Fig. 1. Schematic of a four-point measurement on a heating element with sample

In a typical AC nanocalorimetry experiment, a current with both direct current (DC) and AC components

$$I = I_0 + i\cos(\omega t - \varphi_0) \tag{1}$$

is passed through the resistive heater. The AC component causes the temperature of the heater to oscillate around an average temperature T_0, which increases (in heating) or decreases (in cooling) with time. Hence the temperature response of the heater can be described as

$$T = T_0(t) + \theta(t), \tag{2}$$

where $T_0(t)$ is the average temperature over one oscillation period and $\theta(t)$ represents the oscillating part of the temperature. The amplitude of the oscillation is generally much smaller than the overall rise in temperature of the heater during the experiment. The temperature oscillations cause the resistance of the heating element R to vary as [21]

$$R = R_0(1 + \lambda\theta), \tag{3}$$

where R_0 and λ are the resistance and the thermal coefficient of resistance (TCR) of the heating element at T_0, respectively. The power dissipated by the heater is given by Joule's law,

$$\begin{aligned} P &= I^2 R = [I_0 + i\cos(\omega t - \varphi_0)]^2 R_0(1 + \lambda\theta) \\ &= (I_0^2 + \frac{1}{2}i^2)R_0(1 + \lambda\theta) + 2I_0 i R_0(1 + \lambda\theta)\cos(\omega t - \varphi_0) + \frac{1}{2}i^2 R_0(1 + \lambda\theta)\cos 2(\omega t - \varphi_0) \end{aligned} \tag{4}$$

If $L(T)$ is the rate of heat loss from the heater and sample, then to first order

$$L(T) = L_0(T_0) + \alpha\theta, \tag{5}$$

where $L_0(T_0)$ and α are, respectively, the rate of heat loss at T_0 and its temperature derivative. The heat balance takes the form,

$$P = C\dot{T} + L(T) = C(\dot{T}_0 + \dot{\theta}) + L_0 + \alpha\theta, \tag{6}$$

where C is the total heat capacity of the heating element and the sample. Combining Eqs. (4) and (6) leads to a first-order differential equation in the temperature:

$$\begin{aligned}&(I_0^2 + \frac{1}{2}i^2)R_0(1+\lambda\theta) + 2I_0 iR_0(1+\lambda\theta)\cos(\omega t - \varphi_0) + \frac{1}{2}i^2 R_0(1+\lambda\theta)\cos 2(\omega t - \varphi_0) \\ &= C(\dot{T}_0 + \dot{\theta}) + L_0 + \alpha\theta\end{aligned} \tag{7}$$

To ensure that R_0 remains constant on the time scale of the oscillations, we take

$$\lambda\dot{T}_0 \frac{2\pi}{\omega} \ll 1\,. \tag{8}$$

Furthermore realizing that

$$\lambda\theta \ll 1, \tag{9}$$

because both λ and θ are small, we can reduce Eq. (7) to

$$(I_0^2 + \frac{1}{2}i^2)R_0 + 2I_0 iR_0\cos(\omega t - \varphi_0) + \frac{1}{2}i^2 R_0\cos 2(\omega t - \varphi_0) = C(\dot{T}_0 + \dot{\theta}) + L_0 + \alpha\theta \tag{10}$$

If we take the time average of Eq. (10) over one oscillation period, all oscillating terms vanish and we obtain the following simple equation in T_0

$$(I_0^2 + \frac{1}{2}i^2)R_0 = C\dot{T}_0 + L_0\,. \tag{11}$$

Equation (11) provides the relationship between the DC component of the applied power, the heat loss, and the ramp rate for the average temperature T_0. Subtracting Eq (11) from Eq (10) leads to a first-order ordinary differential equation in θ

$$2I_0 iR_0\cos(\omega t - \varphi_0) + \frac{1}{2}i^2 R_0\cos 2(\omega t - \varphi_0) = C\dot{\theta} + \alpha\theta\,. \tag{12}$$

This equation allows calculation of the oscillating component of the temperature. The temperature T_0 enters Eq. (12) only via the temperature-dependence of R_0, which can be regarded as constant on the time scale of the oscillations by Eq. (8). The steady-state solution to Eq. (12) is given by

$$\theta = \theta_1\cos(\omega t - \varphi_0 - \varphi_1) + \theta_2\cos(2\omega t - 2\varphi_0 - \varphi_2) \tag{13a}$$

$$\theta_1 = \frac{2iI_0R_0 \sin\varphi_1}{C\omega} \tag{13b}$$

$$\theta_2 = \frac{i^2R_0 \sin\varphi_2}{4C\omega} \tag{13c}$$

$$\tan\varphi_1 = \frac{C\omega}{\alpha} \tag{13d}$$

$$\tan\varphi_2 = \frac{2C\omega}{\alpha} \tag{13e}$$

While the applied current has an angular frequency ω only, the temperature oscillation has both ω and 2ω components because the applied power scales with the square of the current. Note that the amplitudes of both components scale inversely with the heat capacity *C*, and that the phases of the temperature oscillations with respect to the applied AC current are increasing functions of the ratio $C\omega/\alpha$. If $C\omega$ is much larger than α, which is true under a broad range of experimental conditions, the phase angles φ_1 and φ_2 approach a value of

$$\varphi_1 \approx \varphi_2 \approx \frac{\pi}{2}. \tag{14}$$

This significantly simplifies the formulas and hence the data analysis. Substituting the expression for θ given by Eq. (13a) into Eq. (3) yields an expression for the resistance of the heating element

$$R = R_0[1 + \lambda\theta_1 \cos(\omega t - \varphi_0 - \varphi_1) + \lambda\theta_2 \cos(2\omega t - 2\varphi_0 - \varphi_2)]. \tag{15}$$

The voltage drop *V* across the heating element is then given by Ohm's law,

$$V = [I_0 + i\cos(\omega t - \varphi_0)]R_0[1 + \lambda\theta_1 \cos(\omega t - \varphi_0 - \varphi_1) + \lambda\theta_2 \cos(2\omega t - 2\varphi_0 - \varphi_2)]. \tag{16}$$

In addition to a DC component, the voltage response has ω, 2ω and 3ω harmonic components. It is useful to deconvolve the voltage response into the four frequency components, V_0, V_ω, $V_{2\omega}$, and $V_{3\omega}$, whose sum is equal to the full voltage response (Eq. 16). The DC component is given by

$$V_0 = I_0R_0 + \frac{1}{2}iR_0\lambda\theta_1 \cos\varphi_1 \approx I_0R_0, \tag{17}$$

while the harmonic components are

$$V_\omega = X_\omega \cos\omega t + Y_\omega \sin\omega t\,, \tag{18a}$$

$$X_\omega = iR_0 \cos\varphi_0 + I_0 R_0 \lambda\theta_1 \cos(\varphi_0+\varphi_1) + \frac{1}{2} iR_0\lambda\theta_2 \cos(\varphi_0+\varphi_2)\,, \tag{18b}$$

$$Y_\omega = iR_0 \sin\varphi_0 + I_0 R_0 \lambda\theta_1 \sin(\varphi_0+\varphi_1) + \frac{1}{2} iR_0\lambda\theta_2 \sin(\varphi_0+\varphi_2)\,, \tag{18c}$$

$$V_{2\omega} = X_{2\omega} \cos(2\omega t) + Y_{2\omega} \sin(2\omega t)\,, \tag{19a}$$

$$X_{2\omega} = \frac{1}{2} iR_0\lambda\theta_1 \cos(2\varphi_0+\varphi_1) + I_0 R_0 \lambda\theta_2 \cos(2\varphi_0+\varphi_2)\,, \tag{19b}$$

$$Y_{2\omega} = \frac{1}{2} iR_0\lambda\theta_1 \sin(2\varphi_0+\varphi_1) + I_0 R_0 \lambda\theta_2 \sin(2\varphi_0+\varphi_2)\,, \tag{19c}$$

$$V_{3\omega} = X_{3\omega} \cos(3\omega t) + Y_{3\omega} \sin(3\omega t)\,, \tag{20a}$$

$$X_{3\omega} = \frac{1}{2} iR_0\lambda\theta_2 \cos(3\varphi_0+\varphi_2)\,, \tag{20b}$$

$$Y_{3\omega} = \frac{1}{2} iR_0\lambda\theta_2 \sin(3\varphi_0+\varphi_2)\,. \tag{20c}$$

In practice, the resistance of the heating element is readily calibrated to temperature, so that T_0 can be determined directly from Eq. (17). According to Eq. (9), the terms containing θ_1 and θ_2 in Eq. (18) are much smaller than terms in iR_0. Thus Eq. (18) cannot generally provide accurate information on the heat capacity. It is possible, however, to determine the heat capacity from either Eq. (19) or (20). Substituting Eqs. (13) and (14) into Eq. (19) and (20) finally yields

$$X_{2\omega} = -(\frac{1}{2} i\theta_1 + I_0\theta_2) R_0\lambda \sin(2\varphi_0) = -\frac{5i^2 I_0 R_0^2 \lambda}{4C\omega} \sin(2\varphi_0)\,, \tag{21a}$$

$$Y_{2\omega} = (\frac{1}{2} i\theta_1 + I_0\theta_2) R_0\lambda \cos(2\varphi_0) = \frac{5i^2 I_0 R_0^2 \lambda}{4C\omega} \cos(2\varphi_0)\,, \tag{21b}$$

$$X_{3\omega} = -\frac{1}{2} iR_0\lambda\theta_2 \sin(3\varphi_0) = -\frac{i^3 R_0^2 \lambda}{8C\omega} \sin(3\varphi_0)\,, \tag{22a}$$

$$Y_{3\omega} = \frac{1}{2} iR_0\lambda\theta_2 \cos(3\varphi_0) = \frac{i^3 R_0^2 \lambda}{8C\omega} \cos(3\varphi_0)\,. \tag{22b}$$

In the adiabatic limit, the heat capacity C can be calculated from the amplitude of the 2ω signal

$$C = \frac{5I_0 i^2 R_0^2 \lambda}{4\omega\sqrt{X_{2\omega}^2 + Y_{2\omega}^2}} = \frac{5I_0 i^2 R_0^2 \lambda}{4\omega |V_{2\omega}|}, \tag{23}$$

or the 3ω signal

$$C = \frac{i^3 R_0^2 \lambda}{8\omega\sqrt{X_{3\omega}^2 + Y_{3\omega}^2}} = \frac{i^3 R_0^2 \lambda}{8\omega |V_{3\omega}|}. \quad (24)$$

Equation (24) reproduces the expression for the heat capacity in the 3ω method used previously for isothermal calorimetry measurements [19]. The 2ω component in the signal and consequently Eq. (23) arise because of the addition of a DC component to the applied current. This DC component provides increased flexibility in choosing the AC frequency and the amplitude of the temperature oscillation. The analysis presented in this section is based on three assumptions described by Eqs. (8), (9) and (14). These equations represent the conditions under which a scanning AC calorimetry measurement can be analyzed using either Eq. (23) or (24). When setting up a measurement, experimental parameters such as the DC and AC currents and the AC frequency need to be selected to satisfy these conditions – a relatively straightforward exercise, as we will show in a later section of this paper.

III. Nanocalorimetric device

A. Description of the device

The nanocalorimetry measurements in this study were performed using a parallel nano-scanning calorimeter (PnSC). The PnSC is a thin-film device described in detail previously [8, 17]. Briefly, it consists of silicon substrate with a 5×5 array of independently controlled micromachined calorimeter cells. Each cell contains a tungsten four-point electrical probe that serves both as a heating element and as a resistance thermometer. The tungsten probe is supported by a freestanding silicon nitride membrane and is completely encapsulated in silicon nitride. Fig. 2a shows a schematic of the cell used for scanning calorimetry measurements in prior work [8], with a thin-film sample deposited in the shaded area between the two sensing leads.

In a typical scanning nanocalorimetry experiment, an electric current is supplied through the tungsten heating element, heating the sample at a rate of approximately 1 - 3×10^4 K/s in vacuum [8]. The fast heating rate mitigates heat loss to the environment and results in a uniform temperature distribution across the sample region [8]. At slower heating rates (<10^3 K/s), however, a large fraction of input power is lost as heat, yielding conditions that are more appropriate for AC calorimetry. In the “strip” heating element design of Fig. 2a the heat loss has an additional

deleterious effect of yielding poor temperature uniformity over the sample region. We enable calorimetry measurements in this heat rate regime by not only employing AC calorimetry, but also incorporating a new device design that provides the necessary temperature uniformity.

This new 'serpentine' device is depicted in Fig. 2b. The length of the heating element is increased by wrapping the heating strip into a 3-fold serpentine. The sample is located on the center strip between the sensing probes. The outer two legs of the heater serve to minimize conductive heat loss to the Si substrate, thus improving the temperature uniformity across the sample region. Fig. 3 shows the full metallization layout of the PnSC device with an array of 25 of these four-point serpentine sensors.

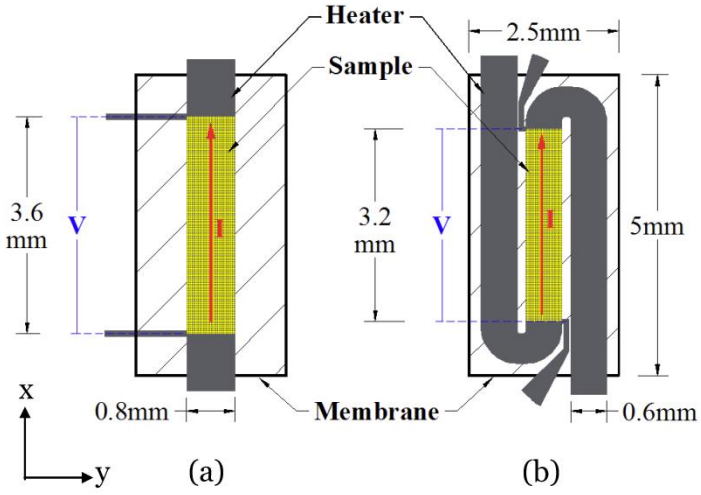

Fig. 2. Layout of the calorimeter cell: strip (a) and serpentine (b)

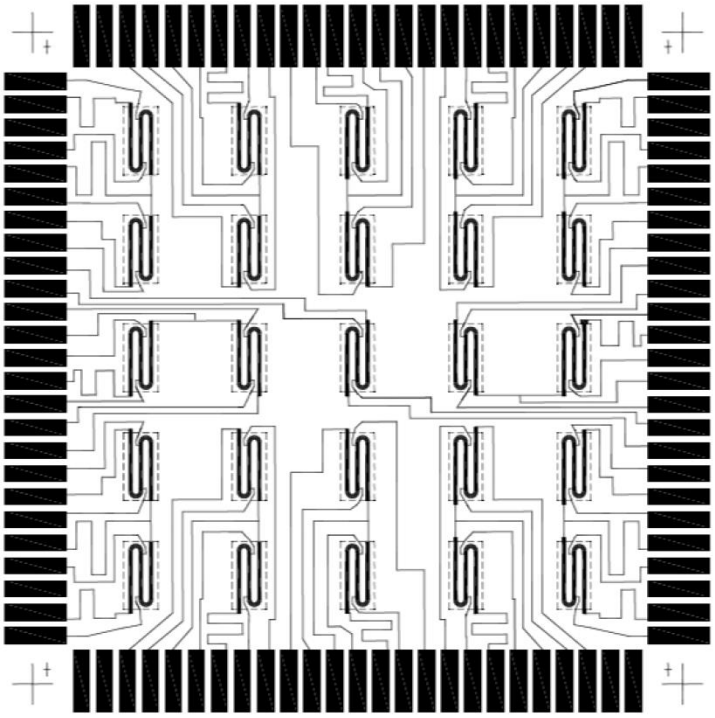

Fig. 3. Metallization layout of the serpentine PnSC device. The lead lines are schematic with reduced width for clarity.

B. Thermal modeling of the calorimetry sensor

To quantify the in-plane temperature distribution in the sample area of the nanocalorimetry sensor, we have constructed finite element models for both the strip and the serpentine designs using the commercial software COMSOL Multiphysics 4.1a. In the *x-y* plane, the models have the same dimensions as the sensors shown in Fig. 2. The models contain a common tungsten thermistor thickness of 125 nm and, where applicable, a tin sample with a thickness of 100 nm. Based on calibrations of actual PnSC sensors, the electrical resistivity of the tungsten heater was modeled as a linearly increasing function of temperature, with a room temperature value of 1.58×10^{-7} Ωm, three times its bulk value, and a thermal coefficient of resistance of 0.00165 K^{-1} [8]. The increase in resistivity above the bulk value is caused by the extremely fine microstructure of the sputtered tungsten. The thermo-physical parameters used in the models are provided in Table 1 and the temperature dependence of these parameters was neglected. The thermal conductivities used in the simulations were one third of their bulk values in accordance with the Wiedemann-Franz law. In a typical experiment, the thermal diffusive length scale is much larger than the physical length scale in the out-of-plane direction, resulting in less than 0.1 K of temperature variation through the thickness of the membrane and the heating element [8, 17]. The small out-of-

plane thermal gradient allowed us to use a more computationally efficient 2-D equivalent model of the device.

The heating process was simulated for sensors with and without the 100 nm tin sample. During the simulation, the boundary of the cell, where the silicon nitride membrane was supported by the silicon wafer, was held at ambient temperature (20^{o}C) because the silicon substrate has a much larger thermal mass than the sensor and it serves as a perfect sink for any heat conducted through the membrane. Both steady-state and time-dependent simulations were conducted. For the steady-state simulations, a constant current was applied to the heater and the corresponding steady-state temperature distribution was determined. By repeating the simulation with currents ranging from low to high, we obtained a series of steady-state temperature distributions with increasing average temperature across the sensor. For the time-dependent simulations, a linearly increasing current was applied to the heating element and the temperature distribution was determined as a function of time. The heating rate was calculated as the time derivative of the average temperature across the sample region. To simulate vacuum conditions, only radiative heat loss with an emissivity ε_c of 0.104 [17] was allowed from the top and bottom surfaces of the sensor. We also performed several steady-state simulations in a He environment, where heat loss occurred by conduction through the He gas in addition to radiation. The conductivity of He was taken to be 0.15 $\mathrm{Wm^{-1}K^{-1}}$ [22]. Convective heat loss was neglected because of the very small Raleigh number.

Typical steady-state simulation results for strip and serpentine devices with a Sn sample are shown in Fig. 4. The temperature distribution in the sample area is clearly much more uniform for the serpentine device than for the strip device in both vacuum and helium environments. The steepest temperature gradients now occur in the outer legs of the serpentine, leaving the center leg and thus the sample region more uniform. The presence of the He improves the temperature distribution in the longitudinal direction, but makes it slightly worse in the transverse direction because of enhanced heat loss from the silicon nitride membrane. To compare the temperature uniformity of different experiments and at different temperatures, we define the relative temperature uniformity, γ, of the sensor as

$$\gamma = \frac{1}{T_0 - T_{RT}} \frac{1}{S} \int |T_0 - T| \, dS' \,, \tag{25}$$

Table I. Parameters used in the FEM models [23-25]

		Length (mm)	Width (mm)	Thickness (nm)	Heat Capacity (J/kg/K)	Thermal conductivity (W/m/K)
Thermistor (W)	Strip	5	0.8	125	132	57.67
	Serp.	15.77	0.6	125		
Membrane ($SiNi_x$)	Strip	5	2.5	125	700	3.2
	Serp.	5	2.5	125		
Sample (Sn)	Strip	3.6	0.8	100	222	22.27
	Serp.	3.2	0.6	100		

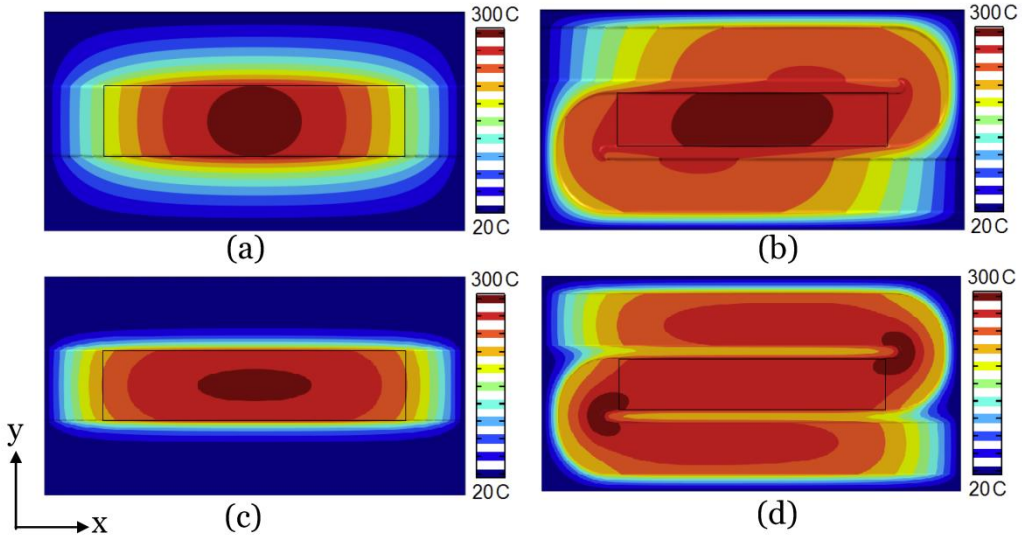

Fig. 4. Typical simulation results for (a) the strip design in vacuum, (b) the serpentine design in vacuum, (c) the strip design in He, and (d) the serpentine design in He. All simulations are for sensors in the steady state with a Sn sample in place. All contour lines are equally spaced. Applied currents are 46 mA, 26 mA, 65 mA and 63 mA, respectively.

where T_{RT} represents room temperature and T_0 is the average temperature across the sample area S. Fig. 5a and 5b show, as a function of average sample temperature, the temperature uniformity in vacuum for three different heating rates. The three heating rates are chosen to represent slow (quasi steady-state), medium (1.5×10^3 K/s) and fast (1.5×10^4 K/s) heating conditions. In most cases, the addition of the sample to the empty sensor improves temperature uniformity due to the enhancement in lateral thermal conduction, which suppresses thermal gradients. Only at very fast

heating rates does the sample degrade the temperature uniformity of the serpentine device slightly. In vacuum, the strip design has good temperature uniformity ($\gamma < 5\%$) for the fastest heating rate, in agreement with previous reports [8]. At slower heating rates, however, the temperature uniformity is significantly degraded mainly because of heat loss to the Si substrate via the tungsten heating element. These results are consistent with prior simulations of strip devices in the steady state [26]. The serpentine design, on the other hand, shows improved temperature uniformity over the entire temperature range and for all heating rates, with γ around 3% at 200°C and decreasing to approximately 1% at 1000°C. We note that the temperature uniformity of the strip design improves significantly as the average temperature increases, because the increased radiative heat loss provides negative feedback for temperature non-uniformity. A similar effect is seen with the He atmosphere (Fig. 5c), with the strip design yielding good temperature uniformity (< 5%) in the steady state, which is a significant improvement compared to the in-vacuum condition. Since the serpentine device already yields good uniformity in the vacuum condition, the addition of He has a relatively small effect.

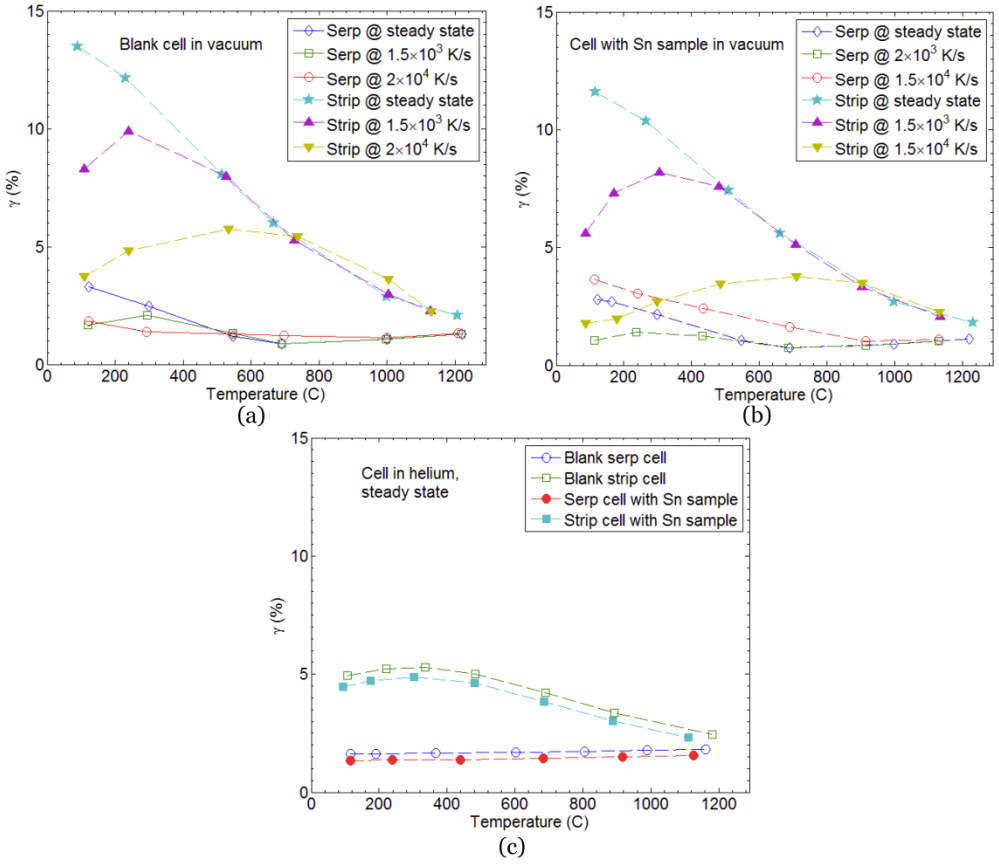

Fig. 5. FEM simulation results: Temperature uniformity γ for (a) blank cells in vacuum, (b) cells with Sn samples in vacuum, and (c) cells in the steady state in He. The heating rates at 300°C is used as the nominal heating rate.

IV. Experimental detail

A. Measurement setup

Fig. 6 shows a schematic of the measurement set up. The PnSC device is installed in a probe card that is mounted inside an ultra-high vacuum (UHV) furnace, with a base pressure of 1e-7 Torr. The UHV furnace is pumped down by a turbo pump (Varian Turbo-V551 Navigator), which is backed by a mechanical pump (Varian TriScroll 300). The furnace provides a chemically inert ambient for the PnSC sensor, enabling measurements in both vacuum and inert gas environments. A custom-designed measurement system serves as a programmable current source and data acquisition (DAQ) system for the PnSC sensors. The systems consists of several sub-systems as illustrated in Fig. 6: (1) A current source with current source controller for powering the PnSC sensors and for monitoring the current output; (2) a DAQ controller for acquiring the voltage output signals from the PnSC sensors; (3) a multiplexer used to select individual sensors for calorimetry measurements by establishing the four electrical connections; (4) an amplifier board for conditioning of the sensor's voltage response and (5) a host interface for executing write/read command from the user computer communicated via an Ethernet cable. The multiplexer consists of a set of mechanical relays, which have negligible crosstalk and near infinite open-state resistance. The host interface communicates to the current source/DAQ controllers through a fiber optic loop and the experiment electronics are powered by low noise DC power supplies (Agilent E3630A and E3620A). The use of fiber optic communication provides galvanic isolation of the experiment circuit from the control electronics. The instrumentation power is also ground-isolated such that the entire experiment circuit is ground-isolated and ground-shielded. The integrated measurement system is controlled via a custom LabView® program on the user computer.

The current source is a modified Howland voltage-to-current converter consisting of three high-precision, low noise operational amplifiers (OPA2227, Texas Instruments, Austin, TX) and a high-output current differential driver (AD815, Analog Devices, Norwood, MA). The current

source has adjustable output ranges (25 mA, 50 mA, 125 mA, 250 mA, and 500 mA) and an output compliance of 25 V. The effective output resistance of the current source is significantly larger than 1 MΩ, which is four orders of magnitude larger than the resistance of the sensors in a typical experiment. A simultaneous-sampling 16-bit per channel ADC/DAC board applies the current program and measures both the applied current (voltage across a precision resistor) and voltage response at a maximum rate of 300 kHz. Each D/A and A/D converter has a memory depth of 1 MB, and is calibrated using precision resistors (Vishay VPR221Z).

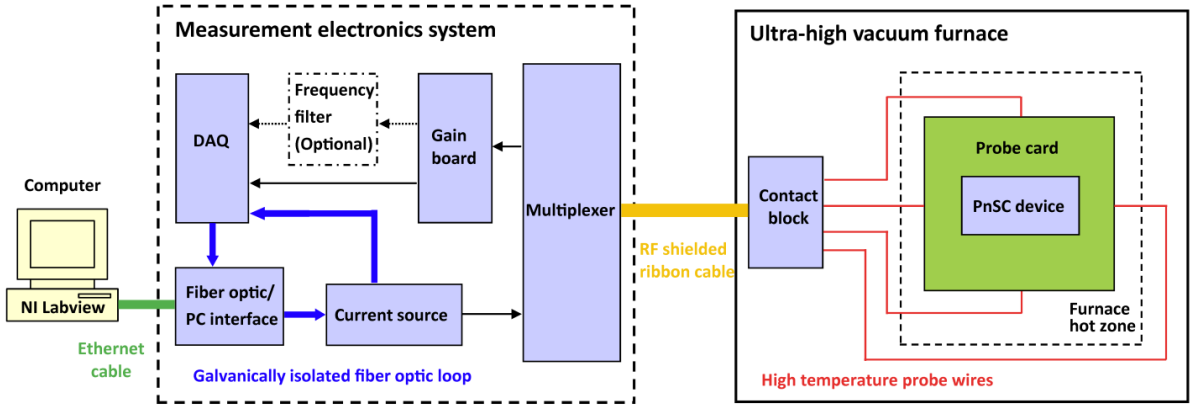

Fig. 6. Schematic of experimental setup.

During a typical measurement, the host interface receives from the user computer a pre-defined digital waveform of input current versus time. A control voltage is sent from the current source controller to the current source, which then passes the analog current through the heating element on the PnSC sensor. The current source controller monitors the input current by measuring the voltage drop across a precision resistor (Vishay VPR221Z) in series with the heating element. The voltage output from the PnSC sensor is amplified and digitized by the DAQ controller. Current input and voltage output from the PnSC sensor are dynamically recorded, stored in digital format in DRAM on the host interface, and transferred to the user computer after completion of the measurement. Analysis of the data occurs in the digital domain, essentially converting the data acquisition system into a digital lock-in amplifier. Detailed circuitry schematics of the data acquisition system are provided as Supplementary Information [27].

B. Device fabrication, calibration, and sample preparation

A PnSC device with serpentine design was fabricated using the same micromachining procedures as for the strip version, described in detail elsewhere [8]. Briefly, the fabrication

process starts with a silicon nitride-coated (100) silicon wafer. Copper metallization and tungsten heating elements are sputter deposited and patterned on the front side of the wafer (Fig. 3), and protected by a thin layer of silicon nitride deposited using plasma enhanced chemical vapor deposition. Rectangular windows are opened in the silicon nitride coating on the backside of the wafer using photolithography and reactive ion etching. The silicon is then etched in a concentrated aqueous KOH solution to make an array of freestanding silicon nitride membranes with tungsten heating elements.

After fabrication, the heating elements of the sensors in the PnSC device need to be calibrated to temperature. The resistance of the heating elements was measured by placing the PnSC device in a vacuum furnace and stepping the furnace temperature from room temperature to 170^{o}C in approximately 15^{o}C intervals. The vacuum furnace was filled with helium gas for better temperature uniformity within the chamber. At each temperature step, a DC current of 1 mA was applied to each heating element on the PnSC device and the voltage across the heating element was recorded. The resistance of the heating elements was found to increase linearly over the entire temperature range. The resistance, R_{RT}, and the thermal coefficient of resistance, λ_{RT}, at room temperature were determined from a linear least squares fit of the resistance data as a function of temperature,

$$R = R_{RT}[1+\lambda_{RT}(T-T_{RT})]. \tag{26}$$

Making the connection with R_0 and λ at temperature T_0, we have

$$\frac{dR}{dT}|_{T_0} = R_0\lambda = R_{RT}\lambda_{RT} \equiv k, \tag{27}$$

where k is defined as the temperature derivative of the resistance. Typical experimental values of R_{RT} and λ_{RT} were 5.37±0.02 Ω and 1.65e-3±2e-5 K^{-1}, respectively.

After calibration of the heating elements, Sn, Bi and In samples were deposited onto the sensors by magnetron sputtering in a centered, on-axis geometry. The deposition was performed using a shadow mask to limit deposition to the center segment of each serpentine sensor. The deposition parameters are summarized in Table II. A quartz crystal monitor was placed into the deposition geometry to measure the mass accumulation rate, from which the total deposited mass was calculated. The thickness values in Table II were calculated assuming standard density of the

elemental solids. After deposition, the deposition mask was removed and an insulating aluminum nitride coating was deposited on all samples under substrate rotation to provide conformal coating. The 32 nm-thick coating was deposited by 89 W of pulsed DC power in a 1.25 Pa atmosphere of 20% N_2 in Ar. The refractory coating provided a protective barrier to oxidation during the calorimetry measurements.

Table II. Sample deposition parameters

material	Ar pressure (Pa)	Power (W)	Rate (nm/s)	Thickness (nm)	Mass (μg)
In	1.3	11	0.25	190	2.6 ± 0.4
Sn	2.4	6	0.14	100	1.4 ±0. 2
Bi	0.67	15	1.1	300	5.6 ± 0.5

C. Experimental procedure and selection of AC measurement parameters

First a series of DC scanning calorimetry measurements were conducted to establish the connection between applied current and heating/cooling rate. Measurements were performed in a 650 mTorr helium atmosphere. Because of the large thermal conductivity of helium and the small thermal mass of the nanocalorimetry sensor (~2 μJ/K), the sensors underwent a quasi steady-state temperature rise with a heating/cooling rate controlled directly by the ramp rate of the applied power. In our experiments, a constant current of 90 mA resulted in a steady-state sensor temperature of approximately 600°C, and by applying an engineered current program, scanning rates ranging from 10 to 2×10^3 K/s for both DC and AC measurements were achieved. By contrast, in a low-heat loss vacuum ambient, a constant current of 90 mA provides a heat rate of approximately 2×10^5 K/s and a steady-state temperature in excess of 1100°C.

Experimental parameters for AC measurements need to be selected to satisfy the conditions spelled out by Eqs. (8), (9) and (14). To better understand how these conditions can be met, we use the results in Eqs. (13) and (27) and substitute them into Eqs. (8), (9) and (14) to yield the following equivalent conditions:

$$\lambda\theta \le \frac{ik}{C\omega}(2I_0 + \frac{1}{4}i) = C_1 \ll 1, \tag{28}$$

$$\frac{k\dot{T}_0}{R_0}\frac{2\pi}{\omega} = C_2 \ll 1, \tag{29}$$

$$\cot\varphi_1 = \frac{\alpha}{C\omega} = C_3 \ll 1. \tag{30}$$

In addition to these conditions, there are a two experimental considerations: 1) the 2ω voltage signal should be at least 20 times greater than the voltage corresponding to the least significant bit of the data acquisition system; 2) the frequency ω must be large enough that the mean temperature rise in a given cycle does not exceed the desired temperature resolution, typically about 2 K [14]. These considerations lead to the following additional conditions

$$\frac{V_{2\omega}}{\xi} = \frac{5i^2 I_0 R_0 k}{4C\omega\xi} = C_4 \geq 20, \tag{31}$$

and

$$\dot{T}_0\frac{2\pi}{\omega} = C_5 \leq 2\mathrm{K}, \tag{32}$$

where ξ is the voltage corresponding to the least significant bit of the data acquisition system. While condition (28) limits the sub-cycle temperature oscillations, we do not state a condition that explicitly limits the instantaneous heating rate. Within a single cycle, the heating rate variations are proportional to $\omega\theta$ and for experiments that are sensitive to the instantaneous heating rate, an additional constraint should be added. Here we considered only the 2ω voltage because that signal is used in the experimental section. Equivalent conditions are easily derived for the 3ω signal. Table III lists typical values of experimental parameters in our experiments. The value of α was determined by estimating the heat loss from a calorimeter cell as a result of radiation and conduction through a helium atmosphere:

$$L = \varepsilon_c\sigma(T^4 - T_{RT}^4)S + \frac{K_{He}}{D}(T - T_{RT})S, \tag{33}$$

$$\alpha = \frac{dL}{dT} = 4\varepsilon\sigma T^3 S + \frac{K_{He}}{D}S, \tag{34}$$

where σ is the Stefan-Boltzmann constant, K_{He} is the thermal conductivity of helium (0.15 $\mathrm{Wm^{-1}K^{-1}}$ [22]), S is the surface area of the calorimeter cell (3.84×10^{-6} $\mathrm{m^3}$), and D is the

distance between cell to the wall of the chamber (~1×10^{-2} m). The value of α increases with temperature and approaches 1.2×10^{-4} W/K^{-1} at 600°C.

It is possible to calculate C and α from the 2ω voltage signal without resorting to the assumption that φ_1 and φ_2 approach the value $\pi/2$ (Eqs. (14) and (30)). This approach requires solving non-linear equations and is not pursued here. These quantities can be computed in a mathematically simpler approach through Fourier analysis of the resistance R, which is readily determined by the ratio of the measured voltage and applied current. This method is, however, not well conditioned when I_0 and i have similar magnitudes, because of the poor signal to noise ratio when the instantaneous applied current approaches zero.

Table III. Typical experimental parameters

C (J/K)	R_{RT} (Ω)	T_0 (C)	k (Ω/K)	$\dot{T}_o$ (K/s)	ξ (V)	α (W/K)
2×10^{-6}	5.6	100-600	9×10^{-3}	10^1 - 10^3	10^{-5}	1.2×10^{-4}

The objective is to find the combination of I_0, i, and frequency $f=\omega/2\pi$ that best satisfies conditions (28) through (32). If the measurement is conducted in a He environment, the heating rate $\dot{T}_o$ is determined solely by the ramp rate of the input power and is independent of the instantaneous values of I_0 and i. Consequently, (29), (30), and (32) are independent requirements for the frequency, that reduce to the following two conditions,

$$f \ll \frac{\alpha}{2\pi C} \approx 9\text{Hz}, \tag{35}$$

$$f \geq \dot{T}_0 \times 0.5\text{K}^{-1}. \tag{36}$$

The minimum frequency used in the experiments is 200 Hz, which readily satisfies condition (35), and additionally satisfies condition (36) for the lowest heating rate of 10 K/s. For the highest range of heating rates, condition (36) prescribes the use of higher frequencies.

Once the appropriate frequency has been selected, it is possible to determine allowable combinations of I_0 and i from conditions (28) and (31). Condition (28) is independent of temperature, while condition (31) becomes somewhat less strict with increasing temperature. Fig.

7 illustrates possible solutions for an AC frequency of 600 Hz. Solid and dotted lines in the figure represent conditions at 80°C and 600°C, respectively. The shaded area represents the locus of permissible combinations of I_0 and i for typical experimental parameters (Table III) at $T_0 = 80$°C. The two red lines are contours of constant average power. For measurements performed in He environments, they also represent equilibrium temperature isotherms. Connecting two points, one on each of the isotherms within the permissible region, with a straight line provides a locus of possible current combinations that leads to a temperature rise from 80 to 600°C. A current program that follows this path through parameter space could provide a quasi-equilibrium sweep in temperature between the two extremes. Engineering of the heating rate is possible by not only varying the rate at which i and I_0 are changed in the experiment, but also by choosing a path that remains in the permissible region and that maintains a monotonically increasing power. Conversely, a controlled-cooling rate experiment can be conducted by choosing a path inside the permissible region that maintains a monotonically decreasing power.

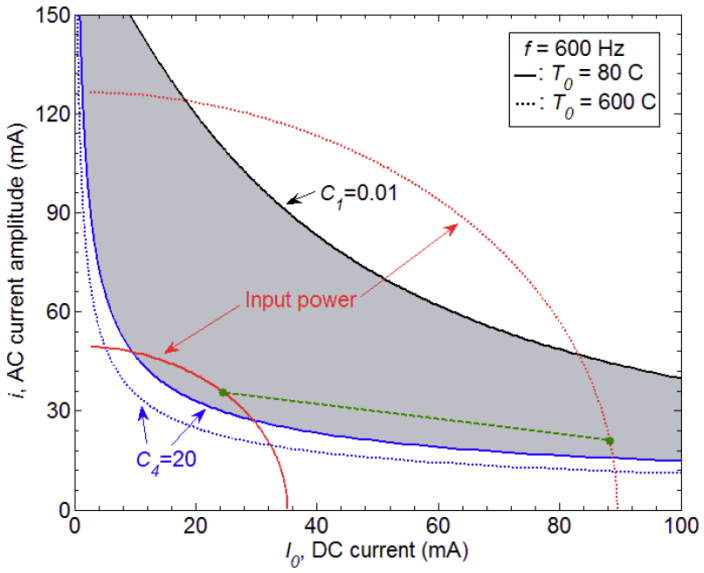

Fig. 7. Geometric solution to inequality set (28) and (31), with experimentally determined input powers for the equilibrium temperature isotherms (red). The C_1 inequality is independent of temperature. The most restrictive contour of the C_4 inequality is used to define the permissible region (shaded area). The curves of constant input power correspond to the 80°C and 600°C isotherms.

D. Data reduction

To analyze the results, the measured currents and voltages for each experiment were divided into segments consisting of an integer number of AC oscillation periods. The signals I_0, i, and V_0 were obtained by performing a discrete Fourier transform (DFT) on every segment of the measured current and voltage, while the voltage. $V_{2\omega}$ was evaluated by first passing the experimental voltage data through a digital band pass filter centered on 2ω and then applying a DFT to every segment. The band pass filter used in the algorithm was a 4th order Butterworth band pass filter with cutoff frequencies 2ω±150Hz. The filter removed the ramping DC component from the voltage data, thus preventing it from entering the windowed Fourier transform calculation and so distorting the $V_{2\omega}$ signal. All discrete Fourier transform were performed using a second order Goertzel algorithm, which is a very efficient method of computing DFT values at specific frequencies [28]. The resistance R_0 was then calculated from V_0 and I_0 according to Eq. (17), and the temperature T_0 was obtained from Eq. (26). The total heat capacity C of a cell was calculated using Eq. (23). Finally, a moving average method was implemented to reduce the noise in the heat capacity results [29].

V. Results and discussion

A. Scanning AC and DC calorimetry measurements

Typical AC calorimetry signals from a PnSC sensor with and without a 100 nm Sn thin-film sample are shown in Fig. 8a; Table IV summarizes the results. The offset between the two signals is caused by the heat capacity of the sample. The difference between the signals normalized by the mass of sample is the specific heat capacity of the sample and is shown in Fig. 8b. The experimental value of the specific heat capacity is 232 ± 20 J/kg K at 100°C and slowly increases to 240 ± 20 J/kg K at 550°C. These results are in good agreement with the literature values for the heat capacity of bulk Sn [30], with the largest contribution to the error arising because of the uncertainty in the sample mass.

The heat capacity shows a peak near the melting temperature of Sn. This peak is caused by melting of the Sn sample, but is not directly related to the latent heat of melting [14, 31]. During the melting process, the AC signal can create oscillations in the relative fraction of the two phases (movement of the phase boundary), which leads to reduced temperature oscillations. This

process is not accounted for in the derivation of Eq. 23 and results in a peak in the AC calculation of the heat capacity [32, 33]. This peak can be used to determine the melting temperature of the sample, but the area under the peak does not correspond to its latent heat of melting as it does in the typical DC analysis. Here, the melting temperature (T_m) is taken at the maximum point of the heat capacity signal [8]. The value for Sn is found to be 230°C, in good agreement with the literature value of 231.9°C [23]. The FWHM of the melting peak is determined mainly by the temperature uniformity of the sensor and the amplitude of the temperature oscillation (2-3K). This is in contrast with traditional calorimetry, where the width of the peak is governed by the heat transfer process between heater, sample, and thermometer, and where the temperature at the onset of the peak is taken as the melting temperature. In fact, in the PnSC, the sample thermally equilibrates with the heater in a time on the order of 10^{-5}s, because of the nanometer-scale distance between the sample and the heating element and the intimate thermal contact between both [8]. At a heating rate of 10^4 K/s, this results in a temperature difference of at most 0.1 K between sample and heating element.

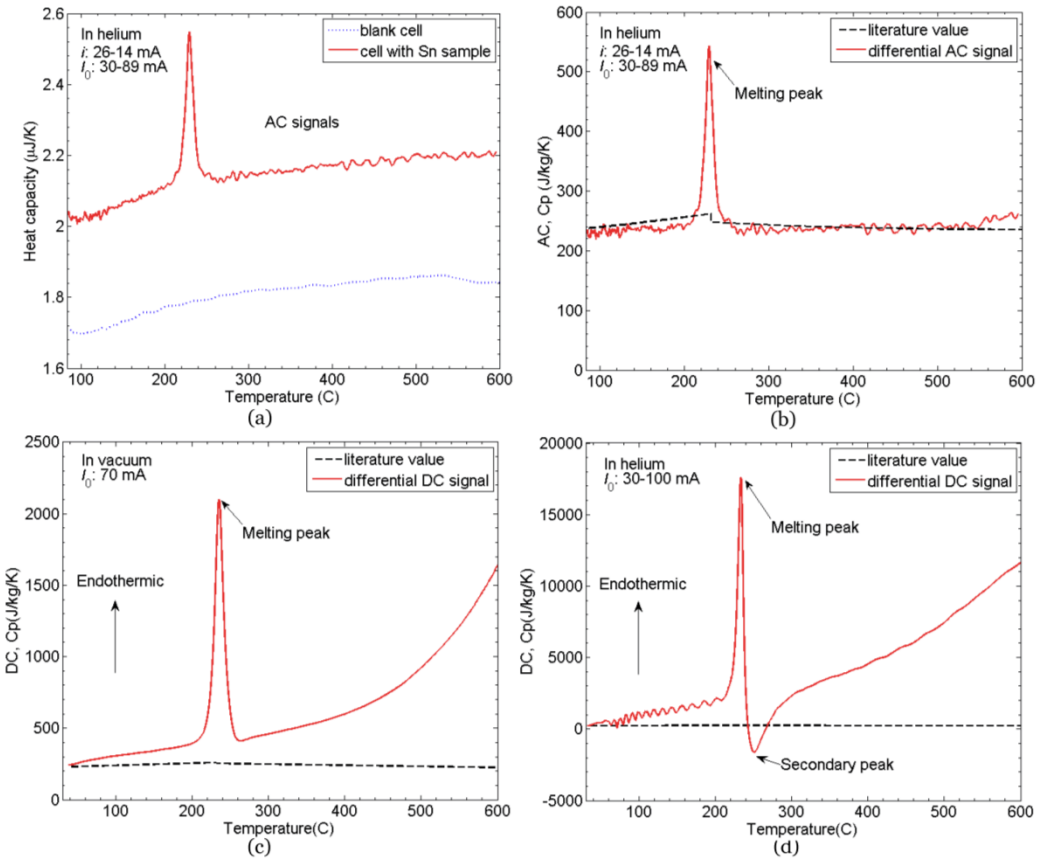

Fig. 8. a) AC calorimetric signals obtained at a scanning rate of 10-10^2 K/s for sensors with and without a 100 nm Sn sample in a He environment using an AC frequency of 666.7 Hz; b) Specific heat capacity of the Sn sample calculated from the AC measurement; c) Specific heat capacity of the Sn sample in vacuum measured at a heating rate of approximately 10^4 K/s using DC calorimetry; d) Specific heat capacity of the Sn sample in He measured at a heating rate of approximately 10^3 K/s using DC calorimetry.

Table IV. Experimental results for Sn sample

Methods	T_m (°C)	FWMH (°C)
AC	230	10.2
DC (fast)	235	8.7
DC (slow)	233	6.9

To illustrate the effect of heat loss on the AC and DC methods, DC measurements were conducted on sensors with and without Sn sample. DC measurements performed in vacuum at a scanning rate of approximately 1.5×10^4 K/s are representative of measurements taken under nearly adiabatic conditions; measurements performed in He at a scanning rate of 10^3 K/s are typical for measurements with significant heat loss to the environment. Results are summarized in Table IV. The specific heat capacities of the Sn sample obtained in these DC measurements are shown in Fig. 8c and 8d; the corresponding heating rate curves are illustrated in Fig. 9. Both for measurements performed in vacuum and in helium, the experimental values of the specific heat capacity agree well with the literature value near room temperature, but they rise quickly with increasing temperature as a result of heat loss to the environment. Part of this heat loss can be eliminated by making a differential measurement, i.e., by taking the difference between a sensor with and without sample, although this procedure is not sufficient to completely take out the effect of the heat loss, even for measurement in vacuum. Allen et al. have developed a more sophisticated technique to remove any heat loss in a DC measurement based on a direct differential measurement between two different sensors [34]. This method works very well if the samples represent a small fraction of the thermal mass of the sensor, which is not the case here. Comparison of the AC (Fig. 8b) and DC measurements (Fig. 8c, 8d) clearly shows that the AC measurement is immune to heat loss, even though the average heating rate in the AC measurement is two orders of magnitude smaller than for the slowest DC measurement (Fig. 9).

The effect of heat loss on DC measurements is further illustrated by comparing Figs. 8c and 8d. In Fig. 8d, the melting peak is followed by what appears to be an exothermic peak, denoted as secondary peak, which is absent in Fig. 8c. The origin of the secondary peak is explained by considering the heat loss from the sample region during and right after melting. During melting, the average temperature of the sample region remains unchanged, while the temperature of the rest of the sensor increases. Consequently, the heat loss from the sample region to the rest of the sensor is slightly smaller at the end of melting process than at the start. Thus, the melting process first causes a dip in the heating rate of the sample, followed by a temporary increase right after melting (Fig. 9). This increase in heating rate produces a secondary, mirrored peak in the heat capacity signal (Fig. 8d). The secondary peak is noticeable whenever the heat loss from the sample region to the rest of the sensor is not negligible compared to the heating power, i.e., in measurements at relatively slow heating rates, and occurs for both endothermic and exothermic reactions. The secondary peak for an endothermic reaction is reflected as an additional exothermic peak in the heat capacity signal, and vice versa for an exothermic reaction. It should be regarded as an experimental artifact that arises because of the sensitivity of DC measurements to non-adiabatic conditions. Unlike DC calorimetry, AC measurements are not affected by heat loss from the sample. Consequently, they do not show a secondary peak in the heat capacity curve, as evident in Figs. 8a and 8b.

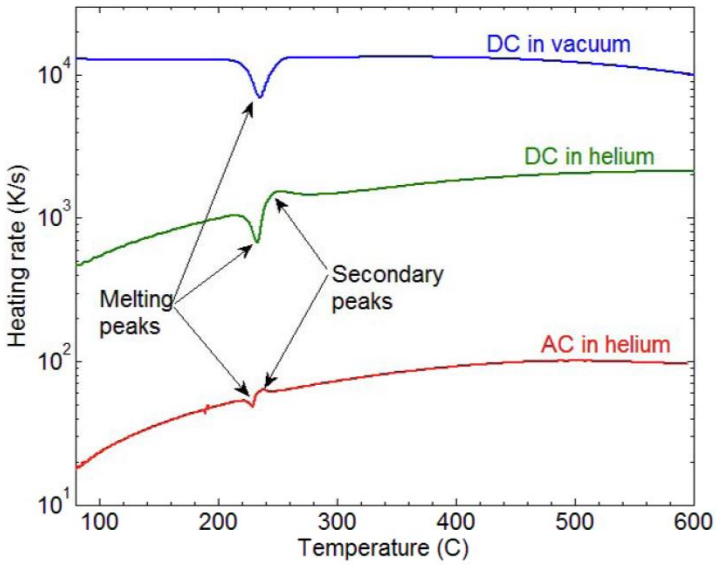

Fig. 9. Heating rates for the AC and DC calorimetric measurements shown in Fig. 8. The heating rate for the AC measurement refers to the cycle-averaged heating rate $\dot{T}_0$.

B. The effect of frequency on the AC measurement

When performing AC calorimetry measurements, it is instructive to explore the frequency dependence of the calorimetry results. AC calorimetry measurements can depend on the frequency at which the measurement is performed for a number of reasons. The thermal wave associated with the AC component of the power decays over a distance $\eta = \sqrt{(K_m/\omega\rho c)}$, where K_m and c are the thermal conductivity and the specific heat capacity of the medium in which the wave propagates, respectively [15, 35]. Consequently, the volume of material – including sample and calorimeter – probed by the thermal wave scales with η. In other words, the volume of material for which the heat capacity is measured, changes inversely with the frequency [36]. Furthermore, the separation distance between the sample and thermometer results in the measured temperature oscillations being damped and delayed with respect to the temperature oscillations of the sample [35, 37]. This effect is negligible if the separation is much smaller than η, but it increases rapidly as the separation exceeds η. As a result, the experimental value of the heat capacity increases with frequency if this effect is not properly accounted for in the analysis. Figs 10a and 10b depict a series of calorimetric signals obtained at different AC frequencies for a sensor with a Sn sample and for a blank sensor, respectively. It is evident from the figures that the experimental values of the heat capacities are virtually identical, independent of measurement frequency, as are the heating rates. This is a direct result of the special geometry of the PnSC device: For typical frequencies, the separation distance between sample and heater/thermometer (~ 100 nm) in the PnSC device is at least an order of magnitude smaller than η so that the measured temperature is an accurate reflection of the temperature of the sample. As the frequency decreases, the value of η increases and sensor samples a larger volume of material, including the He in the ambient and the silicon nitride of the membrane. The results in Figs. 10a and 10b suggest that this effect is negligible. Indeed, the value of η for silicon nitride is 10-30 μm, while that for He is 100-200 μm. The extra mass that lies within these distances from the heater is only a very small fraction of the total sampled mass and thus this frequency-dependent contribution to the heat capacity is negligible. We also note that this measurement artifact is easily removed by calculating the difference signal with the empty device, as was done in Fig. 8b. These results demonstrate that the PnSC sensor is insensitive to the frequency of the AC signal. We do observe that the height of the melting peak in the heat capacity signal increases with

increasing frequency. As described above, this peak is not representative of the specific heat capacity and arises from the quenching of the temperature oscillations due to the coexistence of two phases. In principle the temperature oscillations could vanish during the melting process, providing a divergent heat capacity. A combination of non-equilibrium processes and the sensor's temperature non-uniformity may yield finite temperature oscillations; the windowed Fourier transform data reduction (see Sec. IIID) would require the temperature oscillations to vanish everywhere in the sensor over an entire window to be detected. We assert that the longer time averaging provided by a lower frequency reduces the peak value of the heat capacity signal.

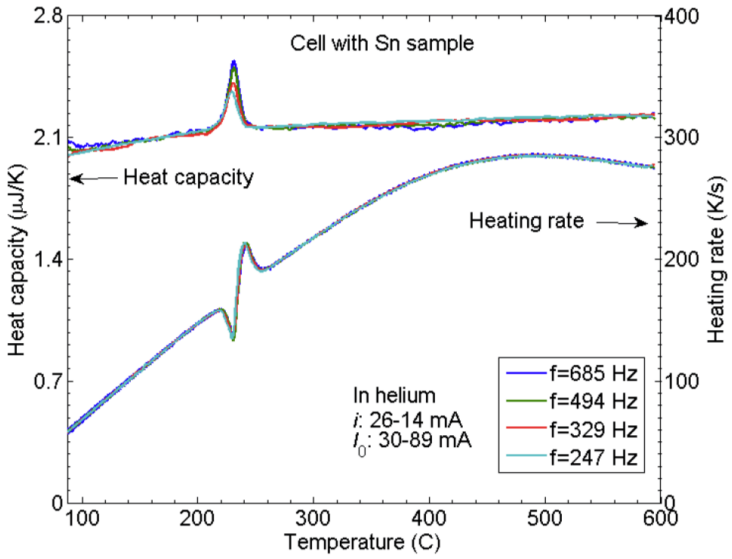

(a)

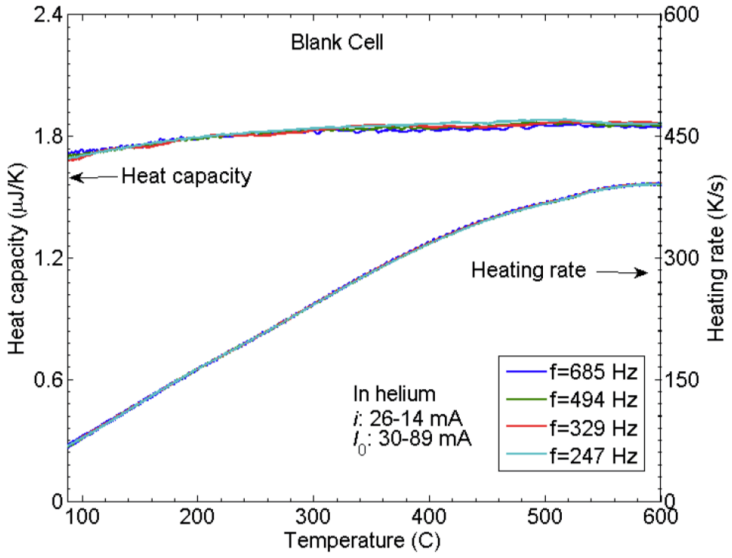

(b)

Fig. 10. Comparison of AC calorimetric signals for different input frequencies: a) cell with a Sn sample; b) blank cell. Input current increased linearly over a period of 3 s. The heating rates refer to the cycle-averaged heating rate $\dot{T}_0$.

C. The effect of scanning rate on the AC measurements

Fig. 11 presents AC calorimetry results obtained at heating rates varying from 10 to 2×10^3 K/s. The experimental values of the heat capacity are independent of the heating rate, with less than 1% difference between their average values. The constancy of the heat capacity demonstrates the capability of the AC technique to perform measurements over a wide range of heating rates. There is a very small increase in melting temperature with increasing heating rate. In traditional calorimetry, such a shift is usually caused by the thermal impedances between heater, sample, and thermometer. In these measurements, these thermal impedances are very small and the temperature difference between sample and heating element is at most 0.1 K. It is therefore more likely that the small shift in melting temperature is caused by a change in the temperature uniformity of the device with heating rate.

As mentioned in Section III, the heating rate for a measurement in He is controlled by how fast the input power increases. Conversely, by decreasing the input power from point B to point A as depicted in Fig. 7, it is possible to cool the sample from 600°C to 80°C at a controlled rate. Fig. 12 shows the AC results on heating and cooling for sensors with 100 nm Sn, In and Bi samples. The heat capacities measured on heating and cooling are in very good agreement. The figure also shows distinct peaks for melting and solidification. In the AC measurements, solidification peaks appear as exothermic peaks, just like melting peaks, because the temperature oscillations are reduced during the solidification process. The result is an apparent increase in the value of *Cp* that is not directly related to the latent heat of the phase transformation. Whether a phase transformation is endothermic or exothermic is, of course, readily determined from the heating rate traces. Note that the peaks for In and Bi are broader than the peak for Sn because these measurements were performed using much larger AC oscillations than for the Sn sample. The measured melting points for In and Bi are 157.1°C and 275°C, respectively. These experimental values are in good agreement with the literature values of 156.6 C and 271.4°C [23]. On cooling, the solidification temperature for In coincides with its melting point, while Bi solidifies at 177.2°C, well below its melting point. There is no sign of a Sn solidification peak over the measured temperature range. We attribute the undercooling of Bi and Sn to kinetically impeded

nucleation of the solid phase. This explanation is in agreement with a recent observation that melted Sn on a graphite substrate can be undercooled as much as 56.1°C below its equilibrium melting temperature when cooled at a rate of 1 K/s [38]. The results in Fig. 12 suggest an undercooling for Sn of at least 132°C below its melting temperature, which is reasonable given that the cooling rate is two orders of magnitude larger than in the previous observation.

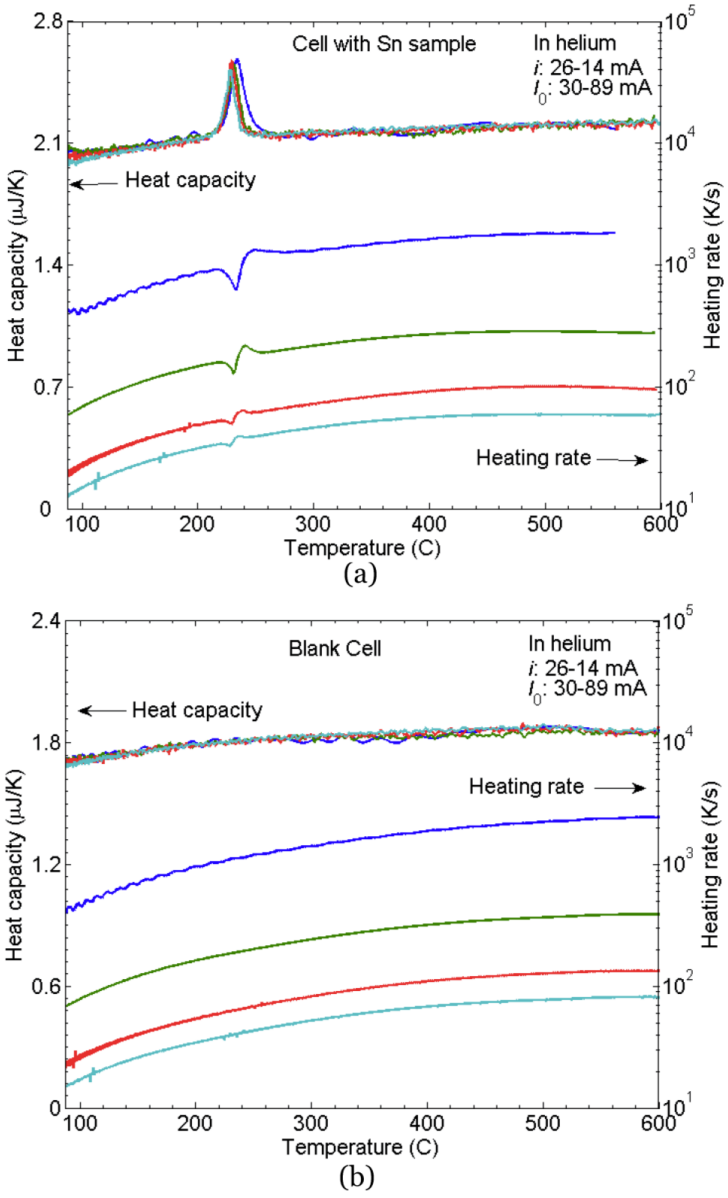

Fig. 11. AC calorimetric signals for different heating rates: a) sensor with a Sn sample; b) blank sensor. Input current increased linearly over a period of 0.5 s, 3 s, and 15 s. The heating rates refer to the cycle-averaged heating rate $\dot{T}_0$.

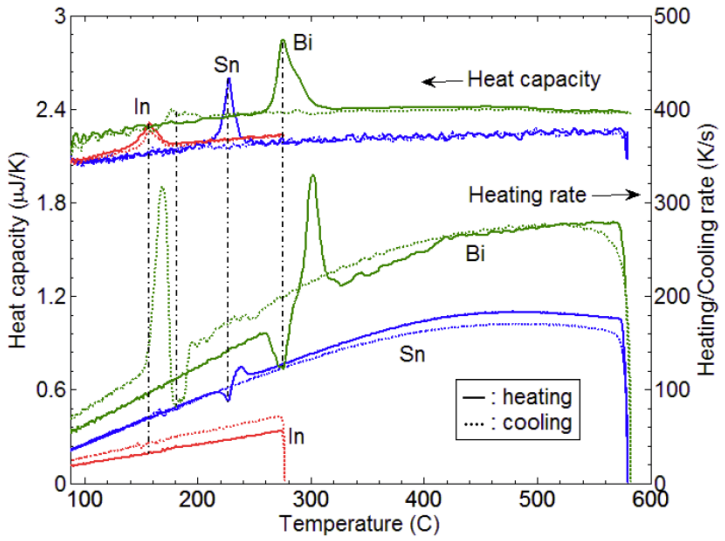

Fig. 12. AC calorimetric signals on heating and cooling for sensors with Sn, In, and Bi samples. The current (I_0, i) for the Sn sample was increased linearly from (30mA, 26mA) to (89mA, 14mA), and then decreased to (30mA, 26mA). The current for In was increased from (31mA, 21mA) to (86mA, 59mA), and then decreased to (13mA, 9mA). The current for Bi was increased from (20mA, 20mA) to (72mA/72mA), and then decreased to (12mA/12mA). The heating rates refer to cycle-averaged heating rate, $\dot{T}_0$.

D. Further discussion

Nanocalorimetry combined with an AC technique makes it possible to obtain calorimetry data for very small quantities of materials over a broad range of heating and cooling rates, currently spanning the range from isothermal to 2×10^3 K/s. The limitation on the maximum scan rate is related to the data acquisition system, rather than the intrinsic properties of the nanocalorimetry device, and is set by the maximum AC frequency that yields an AC response that is both robustly measured within the sample rate of the ADC and is sufficiently large to satisfy inequality (31). We can relax this latter constraint through use of a band pass filter as illustrated in the diagram in Fig. 6. We have implemented an additional A/D channel in the data acquisition system. The sensor voltage signal is copied to this channel and sent through a band pass filter (SR640, Stanford Research Systems) that passes the harmonic signals and filters the relatively large DC and fundamental AC components. The resulting smaller amplitude signal is then amplified, resulting in a much smaller value of ξ. This option will be used in future measurements.

The ability to perform measurements over such a wide range of heating rates, essentially bridging the gap between traditional calorimetry and adiabatic nanocalorimetry, makes AC

nanocalorimetry the ideal technique to study the behavior of materials far from equilibrium. We anticipate that the technique will be useful in the investigation of metallic glasses [5] and in elucidating the role of ultrafine microstructures in phase transformations, to name just a few examples. The broad range of heating rates also makes it possible to study the kinetics of phase transformations and solid-state reactions. Given that the technique is sensitive enough to probe thin-film samples and that it is straightforward to fabricate arrays of sensors, the technique also lends itself for high-throughput analysis of combinatorial libraries and composition spreads. Compared to combinatorial nanocalorimetry [8], the slower scan rates in AC nanocalorimetry make it possible to integrate technique with other characterization methods such as X-ray diffraction in a synchrotron [39], facilitating interpretation of the calorimetry traces.

VI. Conclusion

We have presented an AC nanocalorimetry technique that enables calorimetric measurements on very small quantities of materials over a wide range of heating and cooling rates. Because of the small sample volumes involved, DC nanocalorimetry is quite sensitive to heat loss to the environment and very fast scan rates are required to approach adiabatic conditions. AC calorimetry, by contrast, is much less sensitive to heat loss and can also be used at slow scan rates, as long as the AC frequency is high enough. The AC technique relies on use of the PnSC device, which is an array of micromachined calorimeter sensors. This device is ideally suited for AC measurements because the small thermal impedance between the sample and the heater/thermometer allows the use of frequencies as high as 100 kHz. We have presented an analysis of AC calorimetry specified to the PnSC device and have derived conditions under which valid AC measurements can be obtained. The capability of the technique to make measurements using the PnSC device over a wide range of frequencies and heating/cooling rates is demonstrated by applying it to a 100nm thin-film sample of Sn.

VII. Acknowledgments

The authors would like to thank Jim MacArthur for design and fabrication of the data acquisition system. The work presented in this paper was supported by the Air Force Office of Scientific

Research under Grants FA9550-08-1-0374 and FA9550-12-1-0098, and by the Materials Research Science and Engineering Center at Harvard University. It was performed in part at the Center for Nanoscale Systems, a member of the National Nanotechnology Infrastructure Network, which is supported by the National Science Foundation under NSF Award ECS-0335765. The Center for Nanoscale Systems is part of the Faculty of Arts and Sciences at Harvard University.

Appendix: Validity of AC measurements

To validate the AC measurements, Fig. 13 shows the experimental values of the coefficients C_1 through C_5 in conditions (28) through (32) for a typical AC calorimetry measurement on the Sn sample. C_3 was obtained by applying a Fourier transform to resistance R and by extracting the phase angle φ_1 from its 1ω component. The maximum values for C_1 and C_2 are both well below 0.01. The curve for C_3 peaks near the sample melting temperature with a maximum value of 0.06, which results in a relative error in the amplitude of the 2ω-signal of approximately 0.2% at the melting point and much smaller at other temperatures. These results show that assumptions (28)-(30) in the analysis of the AC signal are readily satisfied. The conditions (31) and (32) imposed by experimental considerations are also met, with $C_4 \approx 20$ and $C_5 < 0.15$ K. Thus the AC measurements and analysis are valid. The largest errors in the measurements arise from uncertainty in the sample mass (15%), the temperature uniformity of the sensor (3%), and the temperature calibration of the heating element (4%).

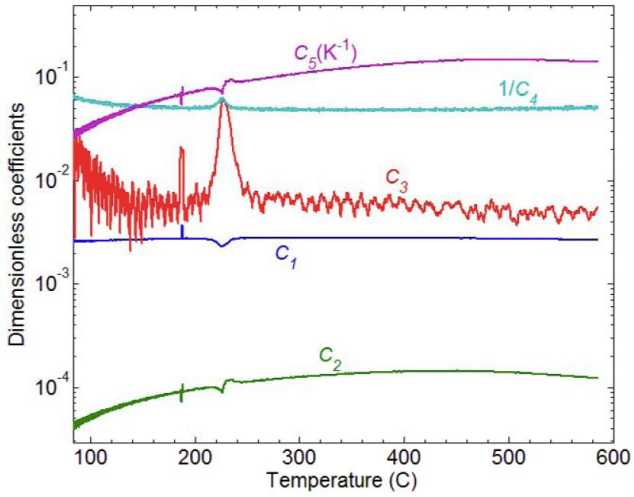

Fig. 13. Experimental results for coefficients *C*1-*C*5. Coefficient C_5 is given in units of Kelvin. The measurement was performed at a heating rate of 10-10^2 K/s and a frequency of 666.7 Hz using a sensor with a Sn sample in a He environment.

References

1. H. E. Kissinger, Analytical chemistry **29** (11), 1702-1706 (1957).
2. S. Lai, G. Ramanath, L. Allen, P. Infante and Z. Ma, Applied physics letters **67**, 1229 (1995).
3. S. L. Lai, J. Y. Guo, V. Petrova, G. Ramanath and L. H. Allen, Physical Review Letters **77** (1), 99-102 (1996).
4. J. Zhang and Y. Zhao, Nature **430** (6997), 332-335 (2004).
5. J. M. Gregoire, P. J. McCluskey, D. Dale, S. Ding, J. Schroers and J. J. Vlassak, Scripta Materialia (2011).
6. T. F. J. Pijpers, V. B. F. Mathot, B. Goderis, R. L. Scherrenberg and E. W. van der Vegte, Macromolecules **35** (9), 3601-3613 (2002).
7. D. Denlinger, E. Abarra, K. Allen, P. Rooney, M. Messer, S. Watson and F. Hellman, Review of Scientific Instruments **65** (4), 946-959 (1994).
8. P. J. McCluskey and J. J. Vlassak, Journal of Materials Research **25** (11), 2086-2100 (2010).
9. M. Y. Efremov, J. Warren, E. Olson, M. Zhang, A. Kwan and L. Allen, Macromolecules **35** (5), 1481-1483 (2002).
10. A. Minakov, S. Adamovsky and C. Schick, Thermochimica Acta **432** (2), 177-185 (2005).
11. P. F. Sullivan and G. Seidel, Physical Review **173** (3), 679-685 (1968).
12. P. Handler, D. Mapother and M. Rayl, Physical Review Letters **19** (7), 356-358 (1967).
13. Y. Kraftmakher, Physics reports **356** (1), 1-117 (2002).
14. A. Lacey, D. Price and M. Reading, Modulated Temperature Differential Scanning Calorimetry, 1-81 (2006).
15. H. Huth, A. A. Minakov and C. Schick, Journal of Polymer Science Part B: Polymer Physics **44** (20), 2996-3005 (2006).
16. A. Minakov, J. Morikawa, T. Hashimoto, H. Huth and C. Schick, Measurement Science and Technology **17** (1), 199-207 (2006).
17. P. J. McCluskey and J. J. Vlassak, Thin Solid Films **518** (23), 7093-7106 (2010).
18. L. A. Rosenthal, Review of Scientific Instruments **32** (9), 1033-1036 (1961).
19. L. R. Holland, Journal of Applied Physics **34** (8), 2350-2357 (1963).
20. C. Dames and G. Chen, Review of Scientific Instruments **76** (12), 124902-124902-124914 (2005).
21. O. M. Corbino, Physik Zeitschr **XI**, 413 (1910).
22. H. Petersen, *The Properties of Helium: Density, Specific Heats, Viscosity, and Thermal Conductivity at Pressures from 1 to 100 Bar and from Room Temperature to about 1800 K*. (Jul. Gjellerup, 1970).
23. T. C. Totemeier and C. J. Smithells, *Smithells metals reference book*. (Butterworth-Heinemann, 2004).
24. R. C. Weast, M. J. Astle and W. H. Beyer, *CRC handbook of chemistry and physics*. (CRC press Boca Raton, FL, 1988).
25. C. H. Mastrangelo, Y. C. Tai and R. S. Muller, Sensors and Actuators A: Physical **23** (1-3), 856-860 (1990).
26. M. Y. Efremov, E. A. Olson, M. Zhang, Z. Zhang and L. H. Allen, Macromolecules **37** (12), 4607-4616 (2004).
27. See supplementary material at [URL will be inserted by AIP] for circuitry diagrams of the electronic measurement system.
28. G. Goertzel, The American Mathematical Monthly **65** (1), 34-35 (1958).
29. A. Savitzky and M. J. E. Golay, Analytical chemistry **36** (8), 1627-1639 (1964).
30. B. J. McBride, S. Gordon and M. A. Reno, 2001. (2001).
31. S. L. Simon, Thermochimica Acta **374** (1), 55-71 (2001).
32. P. R. Garnier and M. B. Salamon, Physical Review Letters **27** (22), 1523-1526 (1971).
33. Y. Saruyama, Journal of Thermal Analysis and Calorimetry **38** (8), 1827-1833 (1992).
34. M. Y. Efremov, E. A. Olson, M. Zhang, S. L. Lai, F. Schiettekatte, Z. S. Zhang and L. H. Allen, Thermochimica Acta **412** (1-2), 13-23 (2004).
35. A. Minakov, S. Roy, Y. Bugoslavsky and L. Cohen, Review of Scientific Instruments **76**, 043906 (2005).
36. T. Suzuki, T. Tsuboi and H. Takaki, Japanese Journal of Applied Physics **21** (2), 368 (1982).
37. A. Minakov, Y. V. Bugoslavsky and C. Schick, Thermochimica Acta **317** (2), 117-131 (1998).
38. J. W. Elmer and E. D. Specht, Journal of Electronic Materials **40** (2), 201-212 (2011).
39. J. M. Gregoire, Xiao, K., Vlassak, J.J., Unpublished.